

The Volatile Inventory of 3I/ATLAS as seen with JWST/MIRI

Matthew Belyakov ,^{1,*} Ian Wong ,^{2,*} Bryce T. Bolin ,³ M. Ryleigh Davis ,¹ Steven J. Bromley ,⁴ Carey M. Lisse ,⁵ and Michael E. Brown 

¹Division of Geological and Planetary Sciences, California Institute of Technology, Pasadena, CA 91125, USA

²Space Telescope Science Institute, 3700 San Martin Drive, Baltimore, MD 21218, USA

³Eureka Scientific, Oakland, CA 94602, USA

⁴Department of Physics, Auburn University, Leach Science Center, Auburn, AL 36849, USA

⁵Johns Hopkins University Applied Physics Laboratory, Planetary Exploration Group, Space Department, 11100 Johns Hopkins Road, Laurel, MD 20723, USA

Abstract

We present the first spectroscopic characterization of an interstellar object at mid-infrared wavelengths. Post-perihelion observations of 3I/ATLAS using the JWST/MIRI medium-resolution spectrometer were obtained on 2025 December 15–16 and 27 when the object was at heliocentric distances of 2.20 and 2.54 au, respectively. Our 5–28 μm spectra exhibit fluorescence features from several gaseous species, including the ν_2 band of H_2O at 5.8–7.0 μm , the primary ν_2 and associated hot bands of CO_2 around 15 μm , and a forbidden transition of atomic nickel at 7.507 μm . We also report the first direct detection of CH_4 in an interstellar object. The delayed onset of CH_4 production relative to H_2O suggests past depletion from the outermost layers, with the observed CH_4 emerging from unprocessed subsurface material. Comparison of the volatile production rates measured during the two epochs indicate a significant reduction in overall outgassing over 12 days, with the measured H_2O activity level dropping more steeply than other species. As shown through near-nucleus coma mapping, 3I continues to display an extended source of H_2O production from icy grains entrained within the coma. Our production rate measurements confirm that 3I exhibits a strongly enhanced $\text{CO}_2:\text{H}_2\text{O}$ mixing ratio relative to typical solar system comets, as well as a somewhat enriched $\text{CH}_4:\text{H}_2\text{O}$ value.

United Astronomy Thesaurus concepts: Interstellar objects (52); Small Solar System bodies (1469); Comet volatiles (2162); Infrared spectroscopy (2285); James Webb Space Telescope (2291)

1. Introduction

Interstellar objects (ISOs) are planetesimals that formed around other stars and were later ejected from their birth systems through gravitational interactions (for a review, see [Fitzsimmons et al. 2024](#); [Jewitt 2024](#)). During their brief transit through our Solar System, ISOs offer discrete glimpses into extrasolar small body populations and provide a valuable point of comparison for assessing commonalities and differences in planetesimal formation processes throughout the galaxy (e.g., [Gibson et al. 2025](#)).

The interstellar comet 3I/ATLAS (hereafter, 3I) is the third confirmed ISO after 1I/'Oumuamua and 2I/Borisov ([Denneau et al. 2025](#)), with an estimated diameter less than 1 km ([Jewitt et al. 2025](#)). In contrast to 1I, which had an inactive appearance ([Meech et al. 2017](#); [Bolin et al. 2018](#)), 3I exhibits significant outgassing (e.g., [Bolin et al. 2025](#); [Chandler et al. 2025](#); [Santana-Ros et al. 2025](#); [Seligman et al. 2025](#)). Its photometric evolution indicates that its coma consists of large, hundred micron sized dust grains ([Jewitt & Luu 2025](#)). Ground-based observations ([Belyakov et al. 2025](#); [de la Fuente Marcos et al. 2025](#); [Kareta et al. 2025](#); [Optom et al.](#)

2025; [Yang et al. 2025](#)) revealed that 3I is redder than 2I ([Jewitt & Luu 2019](#); [Bolin et al. 2020](#)) or typical cometary nuclei ([Lamy et al. 2004](#)). Modeling of galactic dynamics suggests that 3I's excess velocity is consistent with a dynamical age ranging from 3 to 11 Gyr ([Hopkins et al. 2025](#); [Taylor & Seligman 2025](#)).

A concerted effort has been undertaken to characterize the chemical makeup of 3I's coma. Ground-based spectroscopy at visible wavelengths yielded detections of gas-phase cyanogen and atomic nickel ([Hoogendam et al. 2025](#); [Rahatgaonkar et al. 2025](#); [Salazar Manzano et al. 2025](#)), while radio observations by ALMA added methanol and hydrogen cyanide to the molecular inventory ([Roth et al. 2025](#)). Pre-perihelion space-based observations in the near-infrared with JWST and SPHEREx uncovered fluorescence signatures from H_2O , CO_2 , and CO ([Cordiner et al. 2025](#); [Lisse et al. 2025](#)). Post-perihelion SPHEREx measurements indicated a significant increase in CO production and the emergence of an additional emission feature at 3.2–3.4 μm likely due to organics ([Lisse et al. 2026](#)). Further evidence of 3I's evolving activity includes a bluing visible color ([Zhang & Battams 2025](#)) and the apparent asymmetry between its pre- vs. post-perihelion H_2O production trends ([Tan et al. 2026](#)).

In this Letter, we present the first results from our JWST program targeting 3I at mid-infrared wavelengths during

Corresponding author: Matthew Belyakov

* Authors contributed equally to this work.

its outbound trajectory. Observations with the medium-resolution spectrometer (MRS; [Wells et al. 2015](#); [Argyriou et al. 2023](#)) of the Mid-Infrared Instrument (MIRI) were obtained as part of Cycle 4 Director’s Discretionary Time Program #9442 (PI: M. Belyakov). In this work, we focus on characterizing the gas-phase component of 3I’s coma through spectral modeling of the fluorescence bands and mapping of their spatial distribution.

2. JWST/MIRI Observations

The JWST/MIRI MRS instrument consists of four integral field units (IFUs) that operate simultaneously and cover different portions of the MIRI wavelength range (referred to as channels). Three separate grating settings—short (A), medium (B), and long (C)—are needed to construct an uninterrupted spectrum from 5 to 28 μm . Two sets of A/B/C observations requiring six visits in total were included in the observing program to produce two complete mid-infrared spectra of 3I. All observations were executed on 2025 December 15–16. However, two of the observations (1 and 5) suffered from guide star acquisition failures and were repeated on 2025 December 27 with slightly reduced integration times as Observations 13 and 15. A summary of the observing circumstances and viewing geometries for the six successful visits to 3I is provided in [Table 1](#) in the Appendix.

To improve spatial sampling of the coma and guard against cosmic-ray and other detector artifacts, each 3I observation consisted of four dithered exposures. Observations of a nearby empty background field were acquired immediately following each on-target observation. To avoid possible contamination from 3I’s extended coma, the background field was placed 5' away from the target along a vector perpendicular to the anti-sunward direction. The background observations employed a two-point dither pattern to optimize observing time usage, with the same per-dither integration time as the corresponding on-target observations.

Due to the relatively uncertain orbital ephemerides of 3I at the time, the initial set of observations used a wide dither pattern to maximize on-sky coverage. Subsequent astrometry reduced the uncertainty ellipse, and the rescheduled observations on 2025 December 27 used a smaller dither pattern designed for extended objects.

The uncalibrated data were processed using the `jwstspec` tool ([Wong 2025](#)) to produce fully calibrated, background-subtracted, and dither-combined data cubes. [Figure 1](#) shows the wavelength-collapsed Channel 2 data cubes for the six successful observations of 3I. The target was situated close to the edge of the composite field of view in the first three observations. The off-center pointing proved to be problematic for Observation 3, where edge effects introduced significant correlated noise into the measured spectrum; as such, that observation was excluded from the analysis. The coma of 3I extends far beyond the spatial coverage of the MRS observations ([Lisse et al. 2026](#)).

In these close-in views of the near-nucleus region, the dust continuum follows a mostly isotropic spatial distribution, with a slight bias towards the anti-sunward direction, similar to the anti-solar coma direction of 2I/Borisov ([Bolin & Lisse 2020](#); [Kim et al. 2020](#)).

Spectra were extracted from the data cubes using a fixed 1"-diameter circular aperture centered on the target’s centroid position. The chosen diameter ensured that the extraction aperture was fully within the field of view across all observations. The spectra were also corrected for wavelength-dependent aperture flux losses via calibration curves derived from an analogously extracted standard star. For details on the data reduction and spectral extraction methodology, see [Appendix A](#).

The bottom panel of [Figure 1](#) shows the combined spectra of 3I from the two observing epochs: 2025 December 15–16 (blue; Observations 2, 4, 6) and 2025 December 27 (orange; Observations 13, 15). Adjacent spectral segments from different observations showed small flux offsets, which may stem from either short-term variability in the brightness and activity level of the target and/or imperfect aperture flux loss corrections. To produce a continuous spectrum, each individual segments was rescaled to align the flux levels within the overlapping wavelength regions. The systematic difference in flux level between the two epochs reflects the rapid dimming of 3I during its outbound trajectory.

3. Fluorescence Modeling

The JWST/MIRI spectra of 3I reveal a rich collection of emission features from gas fluorescence within the coma. The mid-infrared ro-vibrational bands of H_2O , CO_2 , and CH_4 , as well as the ground-state forbidden transition of monovalent atomic nickel (Ni I) can be seen above the thermal continuum ([Figure 1](#)). For each volatile species, gas production rates Q and rotational temperatures T_{rot} were derived from retrieval fits to the continuum-subtracted spectra using the Planetary Spectrum Generator (PSG; [Villanueva et al. 2018](#)). Model spectra were generated according to the aperture size, viewing geometry, and target ephemeris at the mid-point time of the observations. A full description of the continuum removal and spectral retrieval methodology is provided in [Appendix B](#).

3.1. Water

The mid-infrared contains prominent emission lines between 5.8 and 7.0 μm from the ν_2 vibrational band of gas-phase H_2O . At the spectral resolution of the MRS ($R \sim 3000$), the ro-vibrational lines of the ortho and para nuclear-spin isomers are easily distinguishable. PSG provides separate molecular line lists for ortho- and para- H_2O , enabling direct measurement of the ortho-to-para ratio (OPR).

The ν_3 manifold spans the transition region between grating/channel settings 1B and 1C, which were sampled by Observations 2 and 6 on 2025 December 15–16, yielding

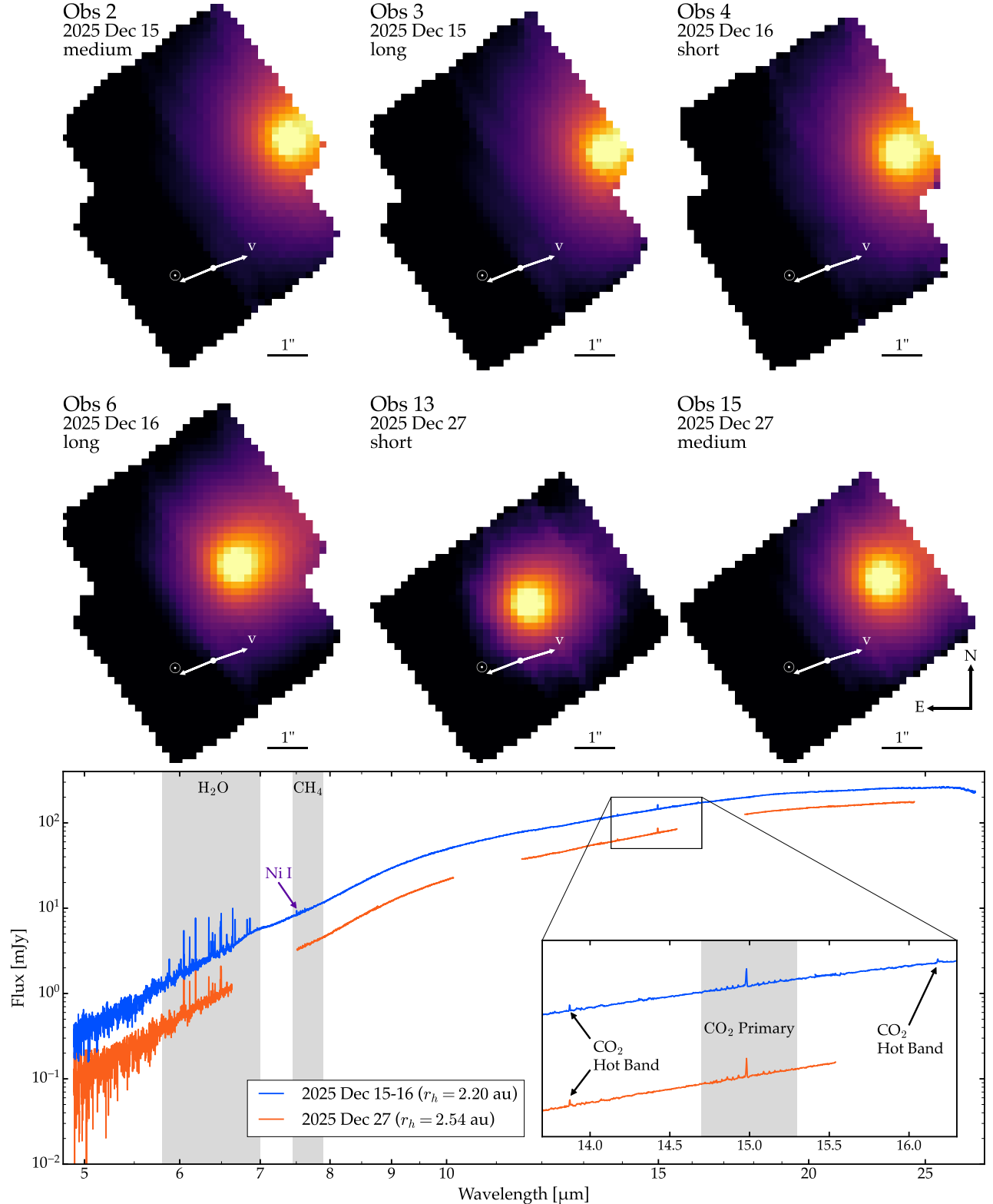


Figure 1. Top panels: median-stacked images derived from the fully calibrated Channel 2 data cubes for the six successful JWST/MIRI observations of 3I. A logarithmic stretch has been applied to accentuate the extended dust coma. The sunward and target velocity directions are indicated. The panels are labeled with the corresponding date and spectral grating setting. Bottom panel: spectra of 3I extracted using a 1''-diameter circular aperture. Observations 2, 4, and 6 (blue) are combined into a single spectrum by normalizing individual segments to align across their overlapping wavelengths. The spectra from Observations 13 and 15 (orange) are unaltered, illustrating the significant decrease in flux as the comet passed from a heliocentric distance of 2.20 au to 2.54 au. The main H_2O , CO_2 , CH_4 , and Ni fluorescence features are marked. The inset panel provides a zoomed-in view of the CO_2 primary and hot bands.

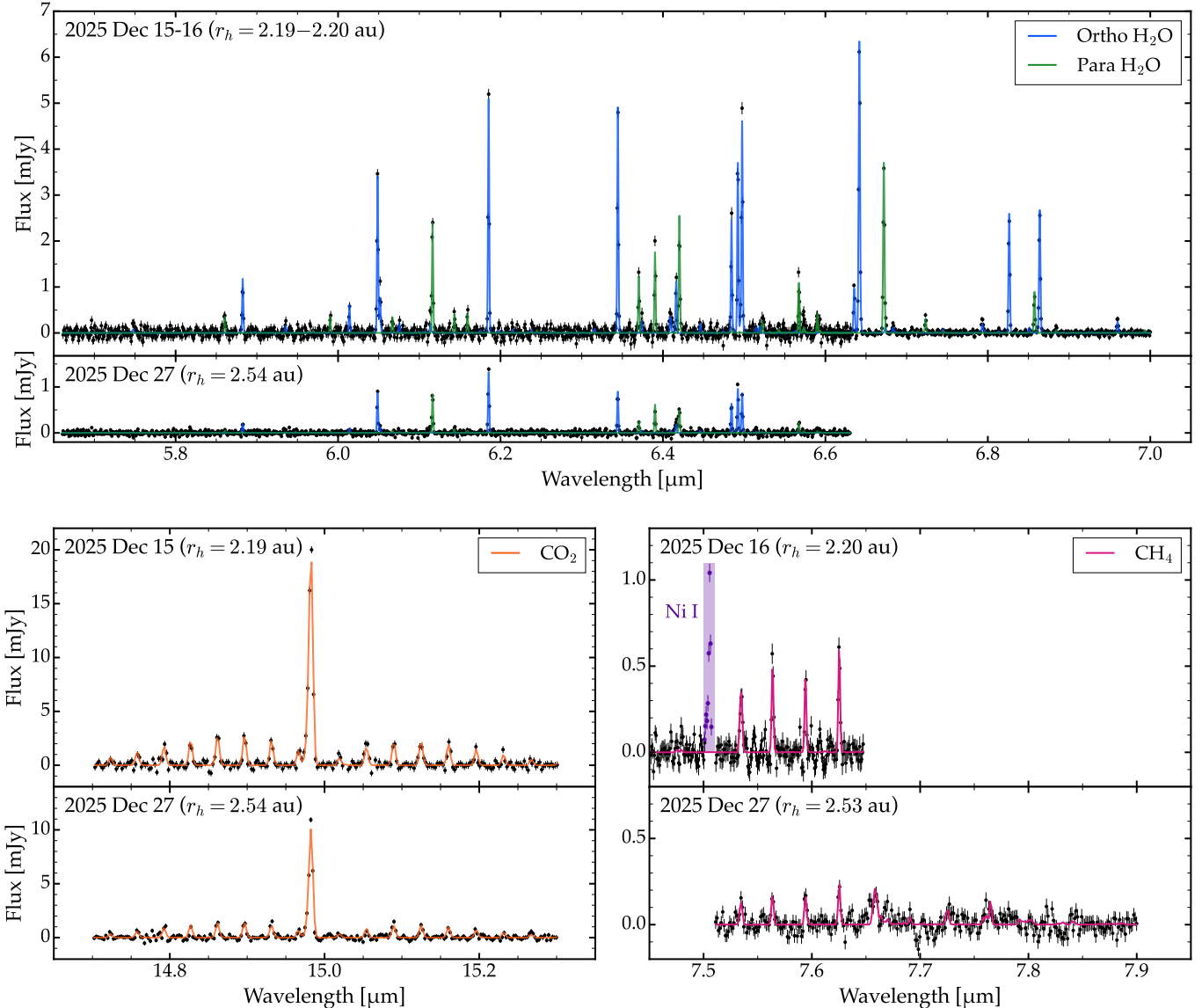


Figure 2. Top panels: continuum-subtracted JWST/MIRI spectra of 3I in the ν_2 band of H₂O from both epochs, with the best-fit PSG coma fluorescence models overlaid. The contributions from ortho- and para-H₂O are shown separately in blue and green, respectively. The line intensities are significantly lower in the second epoch, corresponding to a sizable decrease in H₂O production. Bottom left panels: analogous fits to the ν_2 band of CO₂. Bottom right panels: CH₄ fluorescence model and data. The emission feature highlighted in purple at 7.5066 μm is from the ground-state forbidden transition of Ni I. To illustrate the systematic decrease in production between the two epochs, the vertical scale is identical within each set of panels.

two near-contemporaneous snapshots of 3I's H₂O production. Only the medium grating was used on 2025 December 27 (Observation 15). The three continuum-removed spectra in the H₂O fluorescence region, sorted by epoch, are shown in the top panels of Figure 2.

More than 25 distinct emission peaks are clearly discernible above the noise level in the data from the first epoch. For Observation 2, the ortho- and para-H₂O production rates were $Q_{\text{H}_2\text{O}}^{\text{ortho}} = (2.29 \pm 0.02) \times 10^{27} \text{ s}^{-1}$ and $Q_{\text{H}_2\text{O}}^{\text{para}} = (2.47 \pm 0.05) \times 10^{27} \text{ s}^{-1}$, with a rotational temperature of $T_{\text{rot}} = 33.6 \pm 0.6 \text{ K}$. Results derived from the Observation 6 spectrum are comparable: $Q_{\text{H}_2\text{O}}^{\text{ortho}} = (2.46 \pm 0.01) \times 10^{27} \text{ s}^{-1}$, $Q_{\text{H}_2\text{O}}^{\text{para}} = (2.34 \pm 0.04) \times 10^{27} \text{ s}^{-1}$, and $T_{\text{rot}} = 30.4 \pm 0.4 \text{ K}$.

Meanwhile, a significant reduction in H₂O production is evident in the second epoch, with emission peak amplitudes attenuated by roughly a factor of 4. The PSG retrievals yielded $Q_{\text{H}_2\text{O}}^{\text{ortho}} = (6.86 \pm 0.12) \times 10^{26} \text{ s}^{-1}$, $Q_{\text{H}_2\text{O}}^{\text{para}} = (6.01 \pm 0.25) \times 10^{26} \text{ s}^{-1}$, and $T_{\text{rot}} = 22.2 \pm 0.7 \text{ K}$. The best-fit coma fluorescence models are shown in Figure 2; the ortho- and para-H₂O contributions are plotted in different colors. The models provide an excellent match to the fluorescence peak amplitude distribution across the ν_3 manifold in both observing epochs.

The H₂O isomer line strengths provided by PSG assume an OPR of 3, i.e., the statistical equilibrium value at temperatures above $\sim 40 \text{ K}$. Production rates measured from the retrievals were converted to OPR via the relation OPR =

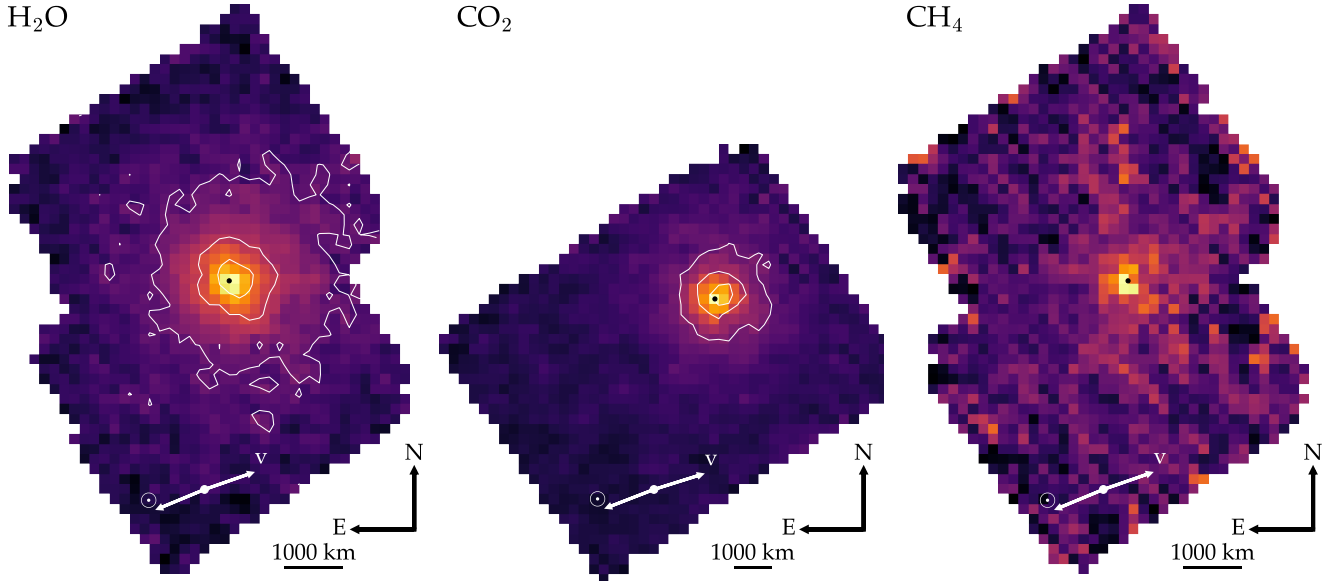


Figure 3. Coma maps of H_2O , CO_2 , and CH_4 , computed as the integrated emission flux across the corresponding fluorescence bands for Observations 6, 15, and 13, respectively. The sunward and target velocity directions are denoted by the white arrows. The target centroids, computed as the photocenter in the median-stacked images (Figure 1), are marked with the black points. For H_2O and CO_2 , the white contours correspond to emission levels of 75%, 50%, and 25% relative to the maximum value and illustrate the slight anti-sunward extension of the respective comae. The precise spatial distribution of CH_4 in the near-nucleus region is poorly constrained due to the low signal-to-noise ratio of the data.

$Q_{\text{H}_2\text{O}}^{\text{ortho}}/Q_{\text{H}_2\text{O}}^{\text{para}} \times 3$. The respective OPR values for the three independent model fits are 2.78 ± 0.06 , 3.15 ± 0.06 , and 3.42 ± 0.15 . Although these values appear to suggest a statistically significant variance in OPR across the three observations, it is important to note that the reported error bars from PSG only reflect the per-point uncertainties of each flux measurement and do not account for correlated noise or systematic uncertainties associated with the continuum removal process. While the production rate and rotational temperature estimates are jointly constrained by the full suite of emission lines, the OPR is highly susceptible to localized noise features, as the ortho- and para- H_2O fluorescence lines have strongly discrepant distributions in wavelength space.

The impact of correlated noise and continuum subtraction methodology was empirically quantified by (1) altering the smoothness threshold of the continuum spline fitting (see Appendix B), and (2) refitting the spectra after iteratively permuting the residual array derived from the best-fit model and adding the shifted array back to the model. The spread of OPR values obtained from this exercise for each of the first epoch observations ranged from 0.2 to 0.3, while the spread was significantly higher (>0.5) for the noisier and lower-precision second epoch spectrum. Given these relatively large systematic uncertainties, all of the retrieved OPR values are consistent with the equilibrium value of 3. Meanwhile, $Q_{\text{H}_2\text{O}}$ values varied by at most 5%, and T_{rot} measurements were consistent to within a few degrees. These variances were found to be similar across different observations and volatile species and can therefore be broadly applied as

representative benchmarks for the systematic errors on Q and T_{rot} values reported throughout this work.

Previous JWST observations of 3I in the near-infrared uncovered evidence of distributed H_2O production within the coma (Cordiner et al. 2025). To assess the impact of an extended H_2O source in the JWST/MIRI dataset and derive so-called terminal $Q_{\text{H}_2\text{O}}$ values that more closely approximate the total H_2O production, an additional set of spectra was measured using a wider 3"-diameter aperture. This analysis was only carried out on Observations 6 and 15 (subbands 1C and 1B, respectively), when 3I was situated near the center of the field of view. In light of the previous discussion, the OPR was fixed to 3. Terminal production rates of $Q_{\text{H}_2\text{O}} = (3.35 \pm 0.02) \times 10^{27}$ and $(8.85 \pm 0.12) \times 10^{26} \text{ s}^{-1}$ were measured for the two epochs.

To visualize the spatial distribution of H_2O production in the vicinity of the nucleus, coma mapping of the integrated fluorescence band intensity was carried out. The spectrum of each spatial pixel within the field of view was extracted, defringed, and continuum-subtracted following the same methodology as the aperture-extracted spectrum. Figure 3 shows the H_2O coma map for Observation 6, which produced the strongest detection of the molecule. The H_2O coma is mostly isotropic, with a marked extension in the anti-sunward direction relative to the target centroid. The H_2O coma morphology mirrors the spatial profile of dust continuum emission (Figure 1). To examine the relative extents of the dust and H_2O emission more closely, azimuthally-averaged radial flux profiles were computed separately for

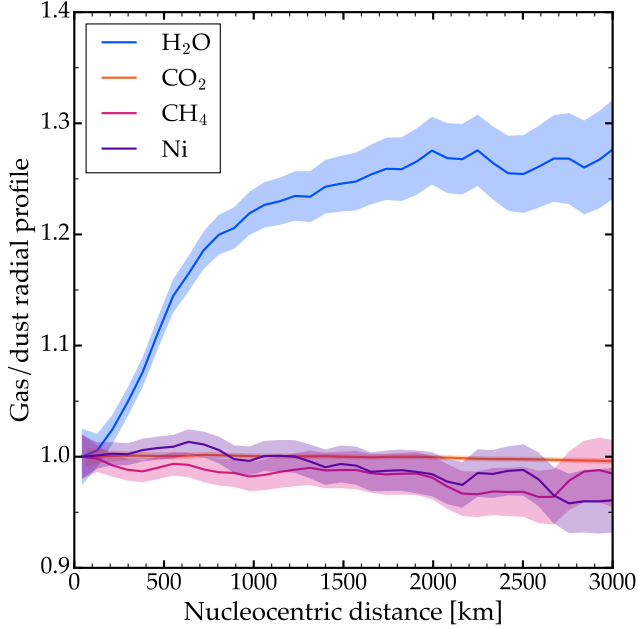


Figure 4. Radial flux profiles of fluorescing gas-phase species normalized to the azimuthally averaged dust radial profile, where the dust profile is measured from wavelength slices adjacent to the emission features. The shading demarcates the 1σ uncertainty regions. Values of 1 indicate that the gas and dust emission follow the same radial dependence, while elevated values suggest an extended source. Only H₂O exhibits a significant deviation from the dust profile, indicating distributed sublimation from icy grains within the coma.

the fluorescence and continuum wavelengths across the ν_2 manifold. The differential radial profile, defined as the ratio between the H₂O and dust profiles, is shown in Figure 4. The significant positive deviation at nucleocentric distances beyond ~ 500 km demonstrates that sublimation of H₂O ice from icy grains lofted into the coma by 3I's activity contributes significantly to the total gas-phase H₂O production (e.g., Cordiner et al. 2025; Tan et al. 2026).

3.2. Carbon Dioxide

Previous observations of 3I have established CO₂ as the primary driver of its activity (Lisse et al. 2025), explaining the reported onset of activity at distances beyond $r_h = 6$ au (Feinstein et al. 2025; Martinez-Palomera et al. 2025). The JWST/MIRI spectra present robust detections of the primary ν_2 bending mode of CO₂ centered at 15 μm , along with the associated hot bands near 13.89 and 16.18 μm (Figure 2). The continuum-subtracted spectra in the CO₂ primary band region are plotted in the bottom left panels of Figure 3. The central Q-branch peak at 14.98 μm is flanked by several lines from the ro-vibrational P- and R-branches.

Retrievals in the primary CO₂ band at 14.7–15.3 μm yielded $Q_{\text{CO}_2} = (1.06 \pm 0.02) \times 10^{28} \text{ s}^{-1}$ and $T_{\text{rot}} = 46 \pm 1 \text{ K}$ for the 2025 December 15 observation, and $Q_{\text{CO}_2} = (6.44 \pm 0.12) \times 10^{27} \text{ s}^{-1}$ and $T_{\text{rot}} = 46 \pm 2 \text{ K}$ on 2025 December 27.

The measured T_{rot} values are statistically identical between the two epochs, while being significantly lower than the reported T_{rot} of ~ 90 K obtained from the previously published analysis of JWST/NIRSpec observations (Cordiner et al. 2025). This discrepancy may be attributed to the low spectral resolution ($R \sim 100$) of the JWST/NIRSpec spectrum, which does not resolve the individual transition lines within the P- and R-branches of the ν_3 asymmetric stretch band at $\sim 4.3 \mu\text{m}$. Given that T_{rot} is primarily determined by the distribution of line amplitudes across the fluorescence manifold, the inability to reliably characterize this distribution can greatly bias the retrieved T_{rot} value. This situation is exacerbated by the optical thickness of the CO₂ coma near the nucleus and the possible presence of an underlying CO₂ ice absorption that could affect the continuum modeling across the fluorescence feature. As of this writing, follow-up JWST/NIRSpec observations of 3I using a higher-resolution grating setting have been collected and will provide a more robust estimate of T_{rot} based on the ν_3 band.

The central region of the CO₂ coma measured by the JWST/MIRI observations is not strictly optically thin, with optical depths rising as high as ~ 0.5 in the first epoch. At these enhanced optical depths, PSG provides a first-order adjustment to the modeled fluorescence lines. However, this correction has only been benchmarked for small phase angles, while the JWST/MIRI observations were obtained at $\alpha > 18^\circ$. As a sanity check for the reported parameter values, a set of retrieval runs was carried out with the opacity correction deactivated following the method of Woodward et al. (2025): after dividing the continuum-removed spectrum by 10 and running the retrieval, the resultant Q_{CO_2} value was multiplied by 10. The production rates assuming an optically thin coma are $Q_{\text{CO}_2} = (9.02 \pm 0.11) \times 10^{27} \text{ s}^{-1}$ and $(5.74 \pm 0.10) \times 10^{27} \text{ s}^{-1}$ for the two epochs. It follows that the relative enhancement of Q_{CO_2} stemming from the PSG optical depth correction is roughly 17% and 12%, respectively. These are relatively minor adjustments in the context of the range of measured production rates across the various volatile species and as such do not have a substantial impact on the scientific results of this work. The following discussion utilizes the opacity-corrected production rates.

The hot bands of CO₂ have not been previously reported on comets, as Spitzer was the only facility covering the mid-infrared wavelengths necessary to observe them, and the relatively low band amplitudes precluded their detection. Recent observations of protoplanetary disks with the JWST/MIRI MRS have measured the two CO₂ hot bands. Modeling of the ν_2 CO₂ manifold observed in GW Lup by Grant et al. (2023) demonstrated that detailed radiative transfer modeling within an optically thick regime is necessary to self-consistently reproduce the amplitudes of the primary and hot bands, which is beyond the scope of this Letter. In the context of 3I, the presence of hot bands suggests that collisionally-induced

pumping of high-energy ro-vibrational levels is likely occurring in the dense innermost region of the CO₂ coma.

The coma map and radial profile of CO₂ measured from the second epoch (Observation 15) are plotted in Figure 3 and Figure 4. It is evident that CO₂ exhibits a much more compact coma than H₂O. The radial profile of 3I at the CO₂ fluorescence wavelengths is consistent with the dust continuum profile across the full range of sampled nucleocentric distances, obviating the need to invoke an extended source within the coma, in line with the findings of Cordner et al. (2025). As in the case of H₂O, the CO₂ coma shows a slight extension in the anti-sunward direction.

3.3. Methane

Four fluorescence peaks of the ν_4 triply degenerate bending mode of CH₄ are evident between 7.50 and 7.65 μm in both the sub-band 1C and 2A spectra obtained in Observations 6 and 13, respectively (see the bottom right panels of Figure 2). This constitutes the first direct detection of CH₄ on any ISO. Near-infrared spectrophotometry of 3I collected by the SPHEREx spacecraft in 2025 December revealed a broad emission signature at 3.2–3.6 μm (Lisse et al. 2026)—a range that contains the ν_1 symmetric stretching band of CH₄. However, SPHEREx lacks the requisite spectral resolving power to identify the specific hydrocarbon producing the spectral feature, as several other major cometary volatiles have fluorescence bands in that region (e.g., methanol, formaldehyde, and ethane).

Spectral retrievals yielded $Q_{\text{CH}_4} = (4.6 \pm 0.2) \times 10^{26} \text{ s}^{-1}$ and $T_{\text{rot}} = 44 \pm 2 \text{ K}$ for the first epoch. By the time of the second epoch, CH₄ production had fallen by almost 50%, while the rotational temperature remained unchanged, following the same general trends seen for CO₂: $Q_{\text{CH}_4} = (2.4 \pm 0.2) \times 10^{26} \text{ s}^{-1}$ and $T_{\text{rot}} = 41 \pm 5 \text{ K}$. The best-fit fluorescence model spectra are plotted in the bottom right panels of Figure 2. Close inspection of the sub-band 2A spectrum reveals marginal detections of weaker emission features beyond 7.65 μm with amplitudes that are consistent with the model. Due to the low amplitude of the CH₄ fluorescence lines, which are at or below the level of noise in the individual pixel spectra, the corresponding coma map is noisy (Figure 3); the location and orientation of the relatively high CH₄ emission region near the nucleus are poorly constrained and vary strongly when adjusting the details of the pixel-by-pixel continuum modeling. As in the case of CO₂, the radial profile of 3I within the CH₄ fluorescence lines is consistent with the dust continuum profile (Figure 4).

3.4. Nickel

Previous detections of fluorescence from gaseous atomic nickel in distant cometary comae (Manfroid et al. 2021) and on 2I (Guzik & Drahus 2021) have raised the question of how gas-phase metal species are produced at temperatures as low as 150 K—well below the sublimation temperature of nickel-

bearing minerals. The short parent lifetime and $1/\rho$ spatial distribution of Ni have been invoked to suggest that atomic Ni is produced from photodissociation of organometallic complexes, e.g. Ni(CO)₄ (Bromley et al. 2021; Guzik & Drahus 2021; Hutsemékers et al. 2021; Manfroid et al. 2021).

On 3I, Ni fluorescence at near-UV and visible wavelengths has been reported by Hoogendam et al. (2025), Hutsemékers et al. (2025), and Rahatgaonkar et al. (2025). Interestingly, while the Ni/Fe ratio was initially found to be extremely elevated from early pre-perihelion measurements (Rahatgaonkar et al. 2025), it has since steeply declined to Sun-like levels (Hutsemékers et al. 2025). However, the absolute production rates remain significantly higher than those observed on solar system comets.

The JWST/MIRI observations access ground-state transitions from some of the lowest-energy levels of atomic Ni. A query for forbidden transitions of Ni I within the NIST Atomic Spectra Database (Kramida et al. 2024) returned six transitions that lie within the MRS wavelength range. The 7.5066 μm line⁶ is clearly seen in the 2025 December 16 spectrum, as shown in Figure 2. No other incontrovertible detections were found. The next brightest line, with a fluorescence efficiency five times weaker than the observed 7.5066 μm line, occurs at 11.307 μm and corresponds to a transition into the upper level of the 7.5066 μm transition. Close inspection of the JWST/MIRI spectra uncovers a marginal ($\sim 1\sigma$) feature at 11.307 μm . A [Ni I] line at 3.119 μm has a comparable fluorescence efficiency to the 7.5066 μm line and should be easily detected by JWST/NIRSpec observations with the medium- or high-resolution spectral grating. Our observations do not provide a measurement of the Fe/Ni ratio, as there are no strong forbidden transitions from Fe I in the MRS wavelength range, except for the 24.04 μm line, which is in a region of the spectrum dominated by thermal emission and significant systematics that preclude its detection.

To compute Ni production rates from the 7.5066 μm line, fluorescence efficiencies (i.e., g -factors) were first calculated following the method described in Bromley et al. (2021). Next, the number of Ni atoms within the spectral extraction aperture is given as

$$N_{\text{atom}} = 4\pi\Delta^2 \underbrace{\frac{F_{\nu}d\lambda}{g \cdot h \cdot \lambda}}_{\# \text{ Density}} \underbrace{\frac{1}{\pi r^2}}_{\text{Aperture}}, \quad (1)$$

where $F_{\nu}d\lambda$ is the integrated line flux in Jy· μm , r is the corresponding extraction radius in distance units, and Δ in the observer distance. Finally, the Haser model provides the ab-

⁶ Upper level: 3d⁸(³F)4s²(³F₃). Lower level: 3d⁸(³F)4s²(³F₄).

solute production rate (Haser et al. 2020):

$$Q_{\text{Ni}} = 2\pi r v N_{\text{molec}} \times \frac{(\gamma_p - \gamma_d)/\gamma_d}{\int_0^{r/\gamma_p} K_0(x) dx - \int_0^{r/\gamma_d} K_0(x) dx}, \quad (2)$$

where γ_d and γ_p are the scale lengths of the daughter and parent in the hypothesized photodissociation reaction (i.e., Ni I and the putative nickel-bearing carbonyl molecule) taken from Bromley et al. (2021), K_0 is the modified zeroth-order Bessel function of the second kind, and $v = 0.8/\sqrt{r_h} = 0.54 \text{ km s}^{-1}$ is the coma expansion velocity (Ootsubo et al. 2012). The resulting production rate is $\log Q_{\text{Ni}} = 23.87 \pm 0.04 \text{ s}^{-1}$. Using a more straightforward $1/r$ fit without accounting for photodissociation of a parent species, which entails removing the final multiplicative factor containing the γ terms from Equation (2), yields a slightly higher production rate of $\log Q_{\text{Ni}} = 24.06 \pm 0.04 \text{ s}^{-1}$.

It is worth noting that all detections of atomic Ni in cometary nuclei to date have probed higher-energy transitions at near-UV wavelengths, in contrast with the low-energy transition observed by JWST/MIRI. The intensity of the $7.5066 \mu\text{m}$ line may incorporate contributions from additional physics in the coma, such as collisions between Ni and H_2O or CO_2 . Furthermore, the population of the upper level of this transition is primarily determined by fluorescence pumping of strong UV lines. Some of the strong UV lines exhibit large uncertainties in their Einstein A coefficients and corresponding absorption rates, suggesting that the g -factor for the $7.5066 \mu\text{m}$ line may be subject to additional uncertainties. Without contemporaneous measurements of the strong UV lines, it is not possible to further refine the abundance measurement of Ni through this singular feature. One feature that is consistent between our mid-infrared observations and the ground-based near-UV spectroscopy is that the spatial distribution of the Ni traces the dust (Hoogendam et al. 2025, 2026), as shown in Figure 4.

Within this context, we briefly examine the implications of the Ni detection on 3I. The common hypothesis is that Ni is trapped in organometallic complexes (either metal carbonyls, or metal-bonded polycyclic aromatic hydrocarbons; Bromley et al. 2021; Manfroid et al. 2021), which produce bare Ni atoms upon photodissociation. Our single observation is consistent with the pre-perihelion value obtained at roughly the same heliocentric distance (Hutsemékers et al. 2025). If this single point is taken to imply symmetric inbound and outbound production rate trends, we can rule out interpretations of the steep heliocentric distance dependence of Ni production as stemming from the comet's long passage through the interstellar medium. A deeper search capturing both the 7.5 and $11.3 \mu\text{m}$ lines would provide a significantly refined Ni abundance during 3I's outbound trajectory and shed light on the steep heliocentric dependence in Ni production observed by Hutsemékers et al. (2025). The symmetric pre- vs. post-perihelion behavior of the production rate and the dust-like

radial profile of Ni (see Figure 4), however, confirm that the metal's production mechanism and source are distinct from canonical volatile release in comets, as suggested by Rahat-gaonkar et al. (2025). The nickel-to-water ratio and nickel-to- CO_2 ratios indicate that the observed Ni emission is expressed from a rather minor reservoir. The solar abundance of nickel relative to oxygen is approximately 0.34% (Lodders 2003). The JWST/MIRI production rates for CO_2 and H_2O suggest 3I releases $2.5 \cdot 10^{28}$ oxygen atoms from the gas, which can be roughly doubled to account for oxygen in the silicates. This crude estimate for the atomic abundance of oxygen yields a Ni/O ratio of 0.002%. Thus, the hypothesized organometallic complexes represent only a fraction of a percent of the total nickel reservoir.

4. Discussion

From a scientific standpoint, the rescheduling of Observations 13 and 15 proved fortuitous, as the 12-day baseline between the two epochs enables a self-consistent assessment of 3I's evolving gas production. Between 2025 December 15–16 and 27, 3I passed from 2.20 to 2.54 au (Table 1), providing two distinct views of the object's volatile production at heliocentric distances not sampled by previous observations. The H_2O , CO_2 , and CH_4 production rates measured from the JWST/MIRI spectra are plotted in the left panel of Figure 5, where the marked decrease in activity between the two epochs is clearly illustrated. Notably, the $Q_{\text{H}_2\text{O}}$ values exhibit a significantly steeper drop between $r_h = 2.20$ and 2.54 au than the other volatiles, which can be attributed to the lower volatility of H_2O compared to CO_2 and CH_4 . The H_2O ice line in the Solar System is located around 2.5 au, and as 3I approached those heliocentric distances in 2025 December, H_2O production from the coldest regions of 3I's surface and coma would have begun to shut off. Meanwhile, although the total production rates of CO_2 and CH_4 were modulated by the decreasing temperature, the production regions of both molecules are expected to have remained fully activated.

Figure 5 shows a collection of published volatile production rates for 3I. The pre-perihelion data points include $Q_{\text{H}_2\text{O}}$ and Q_{CO_2} values calculated from JWST/NIRSpec observations (Cordiner et al. 2025), $Q_{\text{H}_2\text{O}}$ and Q_{CO_2} production rates obtained from SPHEREx spectrophotometry spanning $r_h = 3.01\text{--}3.49 \text{ au}$ (Lisse et al. 2025), and $Q_{\text{H}_2\text{O}}$ measurements derived from observations by the Swift Observatory (Xing et al. 2025). Post-perihelion production rates include 18 $Q_{\text{H}_2\text{O}}$ estimates derived from Lyman- α measurements by the Solar and Heliosphere Observatory (SOHO; Combi et al. 2025) and a $Q_{\text{H}_2\text{O}}$ value from SPHEREx observations spanning $r_h = 1.95\text{--}2.19 \text{ au}$ (Lisse et al. 2026). The JWST/MIRI-derived $Q_{\text{H}_2\text{O}}$ values presented in this Letter continue the steep drop in H_2O production indicated by the other post-perihelion measurements. Notably, both the SOHO and SPHEREx $Q_{\text{H}_2\text{O}}$ values were obtained using large apertures ($> 10^5 \text{ km}$) that are well-suited to capture the full extent of distributed H_2O production

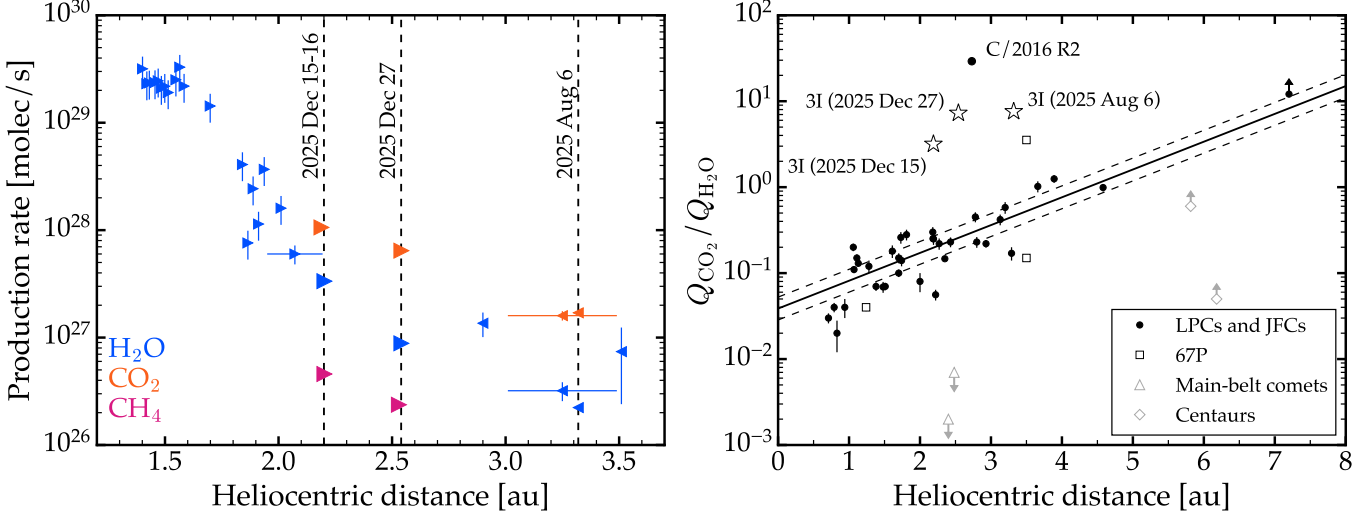


Figure 5. Left panel: a compilation of H_2O , CO_2 , and CH_4 production rates for 3I published in [Combi et al. \(2025\)](#), [Cordiner et al. \(2025\)](#), [Lisse et al. \(2025\)](#), [Xing et al. \(2025\)](#), [Lisse et al. \(2026\)](#), and this work, plotted as a function of heliocentric distance. The JWST epochs (both NIRSpec and MIRI) are marked with vertical dashed lines, and the JWST/MIRI measurements are shown with larger symbols. Left-facing triangles denote pre-perihelion measurements, and vice versa. Right panel: CO_2 -to- H_2O production ratios versus heliocentric distance for various active objects, sorted by dynamical class, with 3I's measurements marked with the star symbols. This plot is a reproduction of Figure 6 in [Cordiner et al. \(2025\)](#) (see reference therein), with the new JWST/MIRI-derived values added. The solid and dashed black lines indicate the best-fit log-linear trend and associated 1σ bounds for the population of long-period comets (LPCs) and Jupiter-family comets (JFCs), excluding the exceptionally CO_2 -rich object C/2016 R2. The measured CO_2 : H_2O mixing ratios for 3I are significantly enriched relative to the trend, though these values may be artificially enhanced due to the limited field of view of the JWST observations. See the discussion for details.

within 3I's expansive coma. It follows that, given the smooth heliocentric distance trend traced by all post-perihelion H_2O production rates, there is no indication that the terminal $Q_{\text{H}_2\text{O}}$ values retrieved from the MRS spectra are significantly underestimating 3I's total H_2O production.

Previous JWST/NIRSpec observations by [Cordiner et al. \(2025\)](#) obtained at $r_h = 3.32$ au found that 3I is unusually rich in CO_2 relative to H_2O reporting a $Q_{\text{CO}_2}/Q_{\text{H}_2\text{O}}$ ratio of 7.3 ± 0.6 . We report $Q_{\text{CO}_2}/Q_{\text{H}_2\text{O}} = 3.17 \pm 0.05$ and 7.28 ± 0.17 for the two epochs of JWST/MIRI spectroscopy, respectively. These ratios were calculated using the terminal $Q_{\text{H}_2\text{O}}$ values measured from the $3''$ -wide aperture in order to account for the extended H_2O production. The right panel of Figure 5 shows an ensemble of published $Q_{\text{CO}_2}/Q_{\text{H}_2\text{O}}$ measurements for active objects (after [Cordiner et al. 2025](#), adding our new mixing ratio measurements). While the heliocentric dependence of $Q_{\text{CO}_2}/Q_{\text{H}_2\text{O}}$ for 3I is roughly similar to that of typical long-period and Jupiter-family comets, 3I's mixing ratio measurements are enhanced by over an order of magnitude relative to most other published values obtained at similar heliocentric distances and approach the CO_2 : H_2O mixing ratio of the exceptionally volatile-rich comet C/2016 R2.

The most notable finding from our mid-infrared spectroscopy of 3I is the robust detection of CH_4 production. As with CO_2 : H_2O , the CH_4 : H_2O mixing ratio of 3I may also be enhanced relative to typical solar system comets. However, previous measurements of the CH_4 production rate for solar system comets beyond $r_h = 2$ au are sparse. Excluding the exceptionally hypervolatile-rich comet C/2016 R2, which has

a reported CH_4 : H_2O mixing ratio of $181\% \pm 25\%$ ([McKay et al. 2019](#)), the handful of published $Q_{\text{CH}_4}/Q_{\text{H}_2\text{O}}$ values spans 0.1 – 10% ([Le Roy et al. 2015](#); [Dello Russo et al. 2016](#); [Bonev et al. 2017](#)). The $Q_{\text{CH}_4}/Q_{\text{H}_2\text{O}}$ values for 3I from the two JWST/MIRI epochs are $13.7\% \pm 0.7\%$ and $27\% \pm 2\%$, respectively, with the higher mixing ratio in the second epoch consistent with the aforementioned pronounced reduction in H_2O outgassing as 3I approached the H_2O sublimation line during its outbound track. Contemporaneous SPHEREx observations on 2025 December 7–15 yielded a CH_4 : H_2O mixing ratio of $\sim 14\%$, assuming that the emission at ~ 3.3 μm is dominated by CH_4 ([Lisse et al. 2026](#)). The agreement between the SPHEREx value, obtained from a large aperture, and the JWST/MIRI measurements suggests that any potential underestimation of $Q_{\text{H}_2\text{O}}$ due to the limited MRS field of view does not have a substantial impact on the reported CH_4 : H_2O mixing ratio.

The delayed onset of CH_4 production raises interesting questions regarding 3I's history. Solid-phase CH_4 is hypervolatile, with a significantly lower sublimation temperature than CO_2 . Thermal modeling of airless bodies (e.g., [Schaller & Brown 2007](#); [Lisse et al. 2022](#)) has demonstrated that CH_4 ice at or near the surface of 3I would have been vigorously sublimating at the time of the first reports of cometary activity during 3I's inbound track ($r_h \sim 6$ au; [Feinstein et al. 2025](#); [Martinez-Palomera et al. 2025](#); [Ye et al. 2025](#)). However, neither the JWST/NIRSpec observations on 2025 August 6 ($r_h = 3.32$ au) nor the SPHEREx spectrophotometry from 2025 August 1–15 ($r_h = 3.01$ – 3.49 au) detected CH_4

fluorescence (Cordiner et al. 2025; Lisse et al. 2025). These observations suggest that CH_4 is depleted in the outermost layers and imply that 3I previously underwent a period of significant heating within its natal planetary system prior to its ejection into the cold interstellar medium (Lisse et al. 2026). Consequently, the surviving reservoir of primordial CH_4 ice resides at depth and was only activated after the thermal wave induced by 3I’s perihelion passage propagated into the interior.

Within this proposed scenario, the early detection of CO outgassing on 3I presents an apparent quandary (Cordiner et al. 2025; Lisse et al. 2025). CO is more volatile than CH_4 and should therefore be depleted from 3I’s near-surface, yet it was detected prior to CH_4 . Recent JWST/NIRSpec observations of Kuiper belt objects (KBOs) provide a plausible resolution to this conundrum. Even at the cold surface temperatures of KBOs (20–40 K), the extreme volatility of CO is such that depletion from the surface occurs on orbital timescales (e.g., Lisse et al. 2022). Nevertheless, a significant subset of mid-sized KBOs (with diameters less than ~ 1000 km) display strong CO ice absorption bands (Brown & Fraser 2023; Pinilla-Alonso et al. 2025). Crucially, solid CO on KBOs appears in conjunction with prominent CO_2 and, in some cases, methanol (CH_3OH) ice features. Lab-

oratory studies demonstrate that CO is a byproduct of CO_2 and CH_3OH radiolysis (e.g., Brucato et al. 1997; Mejía et al. 2015; Quirico et al. 2023; Hénault et al. 2025). It follows that long-term irradiation of icy planetesimals rich in CO_2 may provide a secondary source of surface CO that is stable to sublimative loss within the less volatile matrix of CO_2 ice. On its inbound trajectory, activation of 3I’s surface CO_2 released the trapped CO, thereby explaining the simultaneous observation of CO_2 and CO outgassing prior to the onset of CH_4 activity. Reinterpreting the pre-perihelion JWST/NIRSpec observations of Cordiner et al. (2025) in light of these new results, 3I is most akin to a prototypical CO_2 -type KBO in our Solar System (Brown & Fraser 2023; Holler et al. 2025), ejected from its own system after having undergone a transition similar to the one experienced by Jupiter-family comets (Fraser et al. 2024).

Acknowledgments

We thank Geoff Blake, Carl Schmidt, Zachariah Milby, and Sierra L. Grant for enlightening discussions on spectroscopy. We extend a special thanks to Davide Farnocchia and Marco Micheli for updating the ephemerides of 3I/ATLAS, which allowed these observations to succeed.

Appendix

A. Data Reduction and Spectral Extraction

Table 1 summarizes the exposure details and viewing geometries for the six successful JWST/MIRI MRS observations of 3I collected as part of Program #9442. The apparent magnitude and target distance information are provided for the midpoint time of each set of dithered exposures.

Data reduction and spectral extraction were performed following standard procedures using the publicly-available JWST data analysis tool `jwst spec` (Wong 2025). This data processing framework has previously been applied to numerous JWST observations of small bodies, and detailed descriptions of the pipeline’s functionality can be found in several published works (e.g., Rivkin et al. 2023; Emery et al. 2024; Wong et al. 2024). First, the uncalibrated stacks of non-destructive detector reads were downloaded from the Mikulski Archive for Space Telescopes and passed through all three stages of the official JWST calibration pipeline to produce dark-corrected, flat-fielded, flux-calibrated, spatially-rectified, background-subtracted, and dither-combined data cubes. Fully calibrated data cubes were also generated for each dithered exposure to aid in outlier removal and vet the various molecular signatures detected in the spectra. The pipeline products analyzed in this work were generated using Version 1.20.2 of the JWST calibration pipeline (Bushouse et al. 2025), with requisite reference files drawn from con-

text `jwst_1471.pmap` of the JWST Calibration Reference Data System.

Several custom settings that are not part of the default processing workflow were applied to optimize performance: (1) the cosmic ray detection threshold in the `jump` step in Stage 1 of the calibration pipeline was raised to 10σ to prevent spurious flagging of points in light of the intrinsically variable nature of 3I and possible imperfect non-sidereal tracking of the object during each exposure due to ephemeris uncertainties; (2) the `clean_showers` routine was activated as part of the `straylight` step in Stage 2, which has been shown to greatly mitigate the dispersed flux (so-called showers) that arises from large cosmic ray impacts (Regan 2024); (3) the `residual_fringe` step was performed in Stage 2 to improve the defringing of the flux-calibrated detector images prior to cube building; (4) the `outlier_detection` step was skipped in Stage 3 to prevent erroneous pixel masking during the dither combination process that can often occur with variable moving object targets.

Next, the target centroid was determined by median-averaging the data cube along the wavelength axis and fitting a 2D Gaussian to the flux values within a 5×5 cutout region centered on the brightest pixel in the field of view. Spectra were extracted using $1''$ - and $3''$ -wide fixed circular apertures centered on the centroid position. The angular sizes

Table 1. JWST/MIRI Observation Details and Viewing Geometries

Obs. Numb.	UT Midpoint Time	Grating Setting	Exp. Time (s)	V (mag)	Δ (au)	r_h (au)	α (deg)
2	2025 Dec 15 17:22:40	medium (B)	833	15.31	1.800	2.189	26.68
3	2025 Dec 15 12:49:14	long (C)	833	15.30	1.801	2.181	26.83
4	2025 Dec 16 00:49:25	short (A)	833	15.31	1.800	2.195	26.56
6	2025 Dec 16 06:22:11	long (C)	833	15.32	1.799	2.202	26.43
13	2025 Dec 27 11:20:29	short (A)	777	15.62	1.824	2.530	18.75
15	2025 Dec 27 20:20:30	medium (B)	777	15.63	1.826	2.541	18.46

Note. The reported exposure time is the sum across the four dithered exposures. The variables V , Δ , r_h , and α are the apparent V -band brightness, distance from JWST, heliocentric distance, and phase angle of 3I at the midpoint of the observation as computed by JPL Horizons.

were converted to pixel units using the corresponding pixel scale of each channel: $0.^{\prime\prime}13$ in Channel 1, $0.^{\prime\prime}17$ in Channel 2, $0.^{\prime\prime}20$ in Channel 3, and $0.^{\prime\prime}35$ in Channel 4.

The `jwstspec` tool enables the user to customize the level of outlier rejection in the data cubes prior to spectral extraction. Each pixel flux array within the spectral extraction region is smoothed using a cubic spline fit, and points that exceed a certain multiple of the flux uncertainty σ relative to the spline model are masked as outliers. Given the presence of narrow, large-amplitude emission features in the spectrum of 3I, the outlier rejection threshold was set to a very high value (100σ) to prevent unintentional removal of fluorescence peaks. Likewise, the post-extraction spectral outlier removal threshold, which is applied to a 21-pixel-wide moving median filter, was also set to 100σ to ensure that only extreme non-astrophysical outlier points were excluded.

Remaining outliers in the extracted spectra were manually trimmed in `jwstspec` through careful comparisons with coma fluorescence models (see Appendix B). PSG model spectra were generated for all common cometary volatile species with major emission bands in the mid-infrared, including H_2O , CO_2 , and various aliphatic organic species (e.g., CH_4 , C_2H_6). After identifying the locations of the molecular fluorescence lines, visible outliers were excised across the wavelength regions where no astrophysical spectral features are expected to occur. Lastly, as a final defringing step, the `ifu_rfc` routine contained within the `extract_1d` step of the JWST calibration pipeline was run on the outlier-removed spectra to fit and remove remaining periodic flux variations.

When using a fixed spectral extraction aperture, the fraction of the source flux that falls outside of the aperture shows wavelength-dependent variations due to the changing size of the MIRI point-spread function (PSF). Calibration curves were derived to apply a first-order correction for these flux losses. Observations of the bright A-type standard star HD 2811 and a dedicated background field from Program #7487 were reduced using an analogous procedure to the one described above. After extracting stellar spectra with the same aperture sizes as the ones used for 3I, the individual spectral segments for each channel-grating combination

were divided by the CALSPEC model spectrum of HD 2811 (Bohlin et al. 2014) and fit with cubic polynomials to produce the calibration curves. These correction factors were subsequently applied to the measured spectra of 3I.

The use of calibration curves benchmarked on a point-source observation can yield some bias in the aperture-corrected flux levels for targets that include extended emission. In the case of 3I, the calibration curves address the aperture loss from the point-source-like near-nucleus region, where the vast majority of 3I’s surface brightness is concentrated. Meanwhile, given the smoothly varying nature of the extended continuum emission across the field of view, the fractional aperture loss from the diffuse emission within the extraction region is expected to be largely compensated for by the PSF contribution from points immediately outside of the aperture.

To vet the reliability of the aperture correction, CO_2 and CH_4 production rates were measured from spectra extracted using aperture diameters of $1''$ and $3''$ (Sections 3.2 and 3.3). Previous work has reported that neither of the two molecules show evidence of extended production (Cordiner et al. 2025), and therefore the production rates should not depend on the aperture size. The retrieved CO_2 and CH_4 production rates are consistent between the two aperture diameters, demonstrating that any bias in the aperture-corrected flux levels is negligible and does not have a noticeable impact on the spectral modeling.

B. Spectral Modeling

The PSG (Villanueva et al. 2018) was used to retrieve the production rates and rotational temperatures of the volatile molecular species in 3I’s coma. The online retrieval tool includes a Monte Carlo sampler to calculate the posterior distributions and corresponding 1σ uncertainties for all parameters, which are scaled to ensure a reduced χ^2 value of unity for the best-fit model. To generate the synthetic spectra, the PSG implements the Cometary Emission Model (Villanueva et al. 2022), which accounts for the expansion and evolution of gas molecules through the coma, relevant photodissociation lifetimes, and fluorescence pumping rates within a fully non-local thermal equilibrium (non-LTE) framework. The

line lists for all modeled species were drawn from the GSFC Fluorescence Database (e.g., Villanueva et al. 2011). The coma expansion velocity at each epoch was set according to the scaling law of Ootsubo et al. (2012): $v = 0.8/\sqrt{r_h}$ km s⁻¹.

The viewing geometry (heliocentric distance, observer distance, phase angle) at the midpoint of each observation was queried from JPL Horizons. By default, the wavelength solution contained within the JWST/MIRI data cubes is adjusted to match the target’s stationary frame, and so the radial velocity relative to the observer was set to zero. Imperfections in the wavelength calibration were addressed by allowing for small shifts to the wavelength grid in order to align the model spectra with the observed emission lines. The required shifts were less than 1–2 nm in all cases—comparable to or smaller than the spectral resolution element of the MRS gratings. The synthetic spectra were downsampled to match the local spectral resolution of the modeled data using a Gaussian convolution kernel with a full-width half-maximum scale set by the empirical laws of Pontoppidan et al. (2024) and Banzatti et al. (2025).

To prepare the data for the retrievals, the spectra were trimmed to the fluorescence band regions and continuum-subtracted following a two-step process. First, a crude continuum removal was carried out by fitting a cubic polynomial to the spectra. A preliminary set of retrieval runs was carried out on these spectra, and the corresponding best-fit coma fluorescence models were used to identify the locations of emission lines: all wavelengths with modeled emission amplitudes that exceed a certain fraction of the maximum value within a given band were masked. The masking threshold was set individually for different molecules and observations, pursuant to the characteristic line amplitude distribution and signal-to-noise ratio of the data. For H₂O, a threshold of 0.2% was applied to Observations 2 and 6, while a higher cutoff of 0.5% was used for the noisier Observation 15 spectrum. For CO₂ and CH₄, a limit of 1% was imposed across all observations.

The second, more refined continuum removal step involved an error-weighted cubic spline fit to the masked spectra. The `scipy.interpolate.UnivariateSpline` function includes a smoothing threshold $s = \chi^2$ that controls the performance of the spline fitting. For each modeled fluorescence band, s was adjusted via visual inspection to ensure that the continuum model adequately captures the large-scale modulations in flux without overfitting the point-to-point jitter. The optimal s values ranged from $2n$ to $5n$, where n is the number of continuum data points within the modeled spectral segment. The spline model was subtracted from the unmasked data to yield the continuum-corrected spectra shown in Figure 2.

Facility: JWST/MIRI.

Software: astropy (Astropy Collaboration et al. 2013, 2018, 2022), jwst (Bushouse et al. 2025), jwstspec

(Wong 2025), matplotlib (Hunter 2007), numpy (Harris et al. 2020), PSG (Villanueva et al. 2018), scipy (Virtanen et al. 2020).

References

Argyriou, I., Glasse, A., Law, D. R., et al. 2023, A&A, 675, A111, doi: [10.1051/0004-6361/202346489](https://doi.org/10.1051/0004-6361/202346489)

Astropy Collaboration, Robitaille, T. P., Tollerud, E. J., et al. 2013, A&A, 558, A33, doi: [10.1051/0004-6361/201322068](https://doi.org/10.1051/0004-6361/201322068)

Astropy Collaboration, Price-Whelan, A. M., Sipőcz, B. M., et al. 2018, AJ, 156, 123, doi: [10.3847/1538-3881/aabc4f](https://doi.org/10.3847/1538-3881/aabc4f)

Astropy Collaboration, Price-Whelan, A. M., Lim, P. L., et al. 2022, ApJ, 935, 167, doi: [10.3847/1538-4357/ac7c74](https://doi.org/10.3847/1538-4357/ac7c74)

Banzatti, A., Salyk, C., Pontoppidan, K. M., et al. 2025, AJ, 169, 165, doi: [10.3847/1538-3881/ada962](https://doi.org/10.3847/1538-3881/ada962)

Belyakov, M., Fremling, C., Graham, M. J., et al. 2025, RNAAS, 9, 194, doi: [10.3847/2515-5172/adf059](https://doi.org/10.3847/2515-5172/adf059)

Bohlin, R. C., Gordon, K. D., & Tremblay, P.-E. 2014, PASP, 126, 711, doi: [10.1086/677655](https://doi.org/10.1086/677655)

Bolin, B. T., & Lisse, C. M. 2020, MNRAS, 497, 4031, doi: [10.1093/mnras/staa2192](https://doi.org/10.1093/mnras/staa2192)

Bolin, B. T., Weaver, H. A., Fernandez, Y. R., et al. 2018, ApJL, 852, L2, doi: [10.3847/2041-8213/aaa0c9](https://doi.org/10.3847/2041-8213/aaa0c9)

Bolin, B. T., Lisse, C. M., Kasliwal, M. M., et al. 2020, AJ, 160, 26, doi: [10.3847/1538-3881/ab9305](https://doi.org/10.3847/1538-3881/ab9305)

Bolin, B. T., Belyakov, M., Fremling, C., et al. 2025, MNRAS, 542, L139, doi: [10.1093/mnrasl/sla078](https://doi.org/10.1093/mnrasl/sla078)

Bonev, B. P., Villanueva, G. L., DiSanti, M. A., et al. 2017, AJ, 153, 241, doi: [10.3847/1538-3881/aa64dd](https://doi.org/10.3847/1538-3881/aa64dd)

Bromley, S. J., Neff, B., Loch, S. D., et al. 2021, PSJ, 2, 228, doi: [10.3847/PSJ/ac2dff](https://doi.org/10.3847/PSJ/ac2dff)

Brown, M. E., & Fraser, W. C. 2023, PSJ, 4, 130, doi: [10.3847/PSJ/ace2ba](https://doi.org/10.3847/PSJ/ace2ba)

Brucato, J. R., Palumbo, M. E., & Strazzulla, G. 1997, Icar, 125, 135, doi: [10.1006/icar.1996.5561](https://doi.org/10.1006/icar.1996.5561)

Bushouse, H., Eisenhamer, J., Dencheva, N., et al. 2025, JWST Calibration Pipeline, v1.20.2., Zenodo, doi: [10.5281/zenodo.17515973](https://doi.org/10.5281/zenodo.17515973)

Chandler, C. O., Bernardinelli, P. H., Jurić, M., et al. 2025, arXiv, arXiv:2507.13409, doi: [10.48550/arXiv.2507.13409](https://doi.org/10.48550/arXiv.2507.13409)

Combi, M. R., Mäkinen, T., Berta, J.-L., et al. 2025, arXiv, arXiv:2512.22354, doi: [10.48550/arXiv.2512.22354](https://doi.org/10.48550/arXiv.2512.22354)

Cordiner, M. A., Roth, N. X., Kelley, M. S. P., et al. 2025, ApJL, 991, L43, doi: [10.3847/2041-8213/ae0647](https://doi.org/10.3847/2041-8213/ae0647)

de la Fuente Marcos, R., Alarcon, M. R., Licandro, J., et al. 2025, A&A, 700, L9, doi: [10.1051/0004-6361/202556439](https://doi.org/10.1051/0004-6361/202556439)

Dello Russo, N., Kawakita, H., Vervack, R. J., & Weaver, H. A. 2016, Icar, 278, 301, doi: [10.1016/j.icarus.2016.05.039](https://doi.org/10.1016/j.icarus.2016.05.039)

Denneau, L., Siverd, R., Tonry, J., et al. 2025, MPEC, 2025-N12, doi: [10.48377/MPEC/2025-N12](https://doi.org/10.48377/MPEC/2025-N12)

Emery, J. P., Wong, I., Brunetto, R., et al. 2024, Icar, 414, 116017, doi: [10.1016/j.icarus.2024.116017](https://doi.org/10.1016/j.icarus.2024.116017)

Feinstein, A. D., Noonan, J. W., & Seligman, D. Z. 2025, ApJL, 991, L2, doi: [10.3847/2041-8213/adfd4d](https://doi.org/10.3847/2041-8213/adfd4d)

Fitzsimmons, A., Meech, K., Matrà, L., & Pfalzner, S. 2024, in Comets III, ed. K. J. Meech, M. R. Combi, D. Bockelée-Morvan, S. N. Raymond, & M. E. Zolensky, 731–766, doi: [10.2458/azu_uapress_9780816553631-ch022](https://doi.org/10.2458/azu_uapress_9780816553631-ch022)

Fraser, W. C., Dones, L., Volk, K., Womack, M., & Nesvorný, D. 2024, in Comets III, ed. K. J. Meech, M. R. Combi, D. Bockelée-Morvan, S. N. Raymond, & M. E. Zolensky, 121–152, doi: [10.2458/azu_uapress_9780816553631-ch005](https://doi.org/10.2458/azu_uapress_9780816553631-ch005)

Gibson, A., MacGregor, M. A., Howard, W. S., et al. 2025, ApJL, 993, L29, doi: [10.3847/2041-8213/ae11a1](https://doi.org/10.3847/2041-8213/ae11a1)

Grant, S. L., van Dishoeck, E. F., Tabone, B., et al. 2023, ApJL, 947, L6, doi: [10.3847/2041-8213/acc44b](https://doi.org/10.3847/2041-8213/acc44b)

Guzik, P., & Drahus, M. 2021, *Natur*, 593, 375, doi: [10.1038/s41586-021-03485-4](https://doi.org/10.1038/s41586-021-03485-4)

Harris, C. R., Millman, K. J., van der Walt, S. J., et al. 2020, *Natur*, 585, 357, doi: [10.1038/s41586-020-2649-2](https://doi.org/10.1038/s41586-020-2649-2)

Haser, L., Oset, S., & Bodewits, D. 2020, *PSJ*, 1, 83, doi: [10.3847/PSJ/abc17b](https://doi.org/10.3847/PSJ/abc17b)

Hénault, E., Baklouti, D., Brunetto, R., et al. 2025, *Icar*, 441, 116669, doi: [10.1016/j.icarus.2025.116669](https://doi.org/10.1016/j.icarus.2025.116669)

Holler, B. J., Brunetto, R., Cruikshank, D. P., et al. 2025, *RNAAS*, 9, 241, doi: [10.3847/2515-5172/ae03a2](https://doi.org/10.3847/2515-5172/ae03a2)

Hoogendam, W. B., Shappee, B. J., Wray, J. J., et al. 2025, arXiv, arXiv:2510.11779, doi: [10.48550/arXiv.2510.11779](https://doi.org/10.48550/arXiv.2510.11779)

Hoogendam, W. B., Jones, D. O., Yang, B., et al. 2026, arXiv e-prints, arXiv:2601.16983. <https://arxiv.org/abs/2601.16983>

Hopkins, M. J., Dorsey, R. C., Forbes, J. C., et al. 2025, *ApJL*, 990, L30, doi: [10.3847/2041-8213/adfbf4](https://doi.org/10.3847/2041-8213/adfbf4)

Hunter, J. D. 2007, *CSE*, 9, 90, doi: [10.1109/MCSE.2007.55](https://doi.org/10.1109/MCSE.2007.55)

Hutsemékers, D., Manfroid, J., Jehin, E., Opitom, C., & Moulane, Y. 2021, *A&A*, 652, L1, doi: [10.1051/0004-6361/202141554](https://doi.org/10.1051/0004-6361/202141554)

Hutsemékers, D., Manfroid, J., Jehin, E., et al. 2025, arXiv, arXiv:2509.26053, doi: [10.48550/arXiv.2509.26053](https://doi.org/10.48550/arXiv.2509.26053)

Jewitt, D. 2024, arXiv e-prints, arXiv:2407.06475, doi: [10.48550/arXiv.2407.06475](https://doi.org/10.48550/arXiv.2407.06475)

Jewitt, D., Hui, M.-T., Mutchler, M., Kim, Y., & Agarwal, J. 2025, *ApJL*, 990, L2, doi: [10.3847/2041-8213/adf8d8](https://doi.org/10.3847/2041-8213/adf8d8)

Jewitt, D., & Luu, J. 2019, *ApJL*, 886, L29, doi: [10.3847/2041-8213/ab530b](https://doi.org/10.3847/2041-8213/ab530b)

—. 2025, *ApJL*, 994, L3, doi: [10.3847/2041-8213/ae1832](https://doi.org/10.3847/2041-8213/ae1832)

Kareta, T., Champagne, C., McClure, L., et al. 2025, *ApJL*, 990, L65, doi: [10.3847/2041-8213/adfbdf](https://doi.org/10.3847/2041-8213/adfbdf)

Kim, Y., Jewitt, D., Mutchler, M., et al. 2020, *ApJL*, 895, L34, doi: [10.3847/2041-8213/ab9228](https://doi.org/10.3847/2041-8213/ab9228)

Kramida, A., Yu. Ralchenko, Reader, J., & and NIST ASD Team. 2024, NIST Atomic Spectra Database (ver. 5.12), [Online]. Available: <https://physics.nist.gov/asd> [2016, January 31]. National Institute of Standards and Technology, Gaithersburg, MD.

Lamy, P. L., Toth, I., Fernandez, Y. R., & Weaver, H. A. 2004, in Comets II, ed. M. C. Festou, H. U. Keller, & H. A. Weaver, 223

Le Roy, L., Altweig, K., Balsiger, H., et al. 2015, *A&A*, 583, A1, doi: [10.1051/0004-6361/201526450](https://doi.org/10.1051/0004-6361/201526450)

Lisse, C. M., Gladstone, G. R., Young, L. A., et al. 2022, *PSJ*, 3, 112, doi: [10.3847/PSJ/ac6097](https://doi.org/10.3847/PSJ/ac6097)

Lisse, C. M., Bach, Y. P., Crill, B. P., et al. 2025, arXiv, arXiv:2512.07318, doi: [10.48550/arXiv.2512.07318](https://doi.org/10.48550/arXiv.2512.07318)

Lisse, C. M., Bach, Y., Bryan, S. A., et al. 2026, arXiv e-prints, arXiv:2601.06759, doi: [10.48550/arXiv.2601.06759](https://doi.org/10.48550/arXiv.2601.06759)

Lodders, K. 2003, *ApJ*, 591, 1220, doi: [10.1086/375492](https://doi.org/10.1086/375492)

Manfroid, J., Hutsemékers, D., & Jehin, E. 2021, *Natur*, 593, 372, doi: [10.1038/s41586-021-03435-0](https://doi.org/10.1038/s41586-021-03435-0)

Martinez-Palomera, J., Tuson, A., Hedges, C., et al. 2025, *ApJL*, 994, L51, doi: [10.3847/2041-8213/ae1f91](https://doi.org/10.3847/2041-8213/ae1f91)

McKay, A. J., DiSanti, M. A., Kelley, M. S. P., et al. 2019, *AJ*, 158, 128, doi: [10.3847/1538-3881/ab32e4](https://doi.org/10.3847/1538-3881/ab32e4)

Meech, K. J., Weryk, R., Micheli, M., et al. 2017, *Natur*, 552, 378, doi: [10.1038/nature25020](https://doi.org/10.1038/nature25020)

Mejía, C., Bender, M., Severin, D., et al. 2015, *Nuclear Instruments and Methods in Physics Research B*, 365, 477, doi: [10.1016/j.nimb.2015.09.039](https://doi.org/10.1016/j.nimb.2015.09.039)

Ootsubo, T., Kawakita, H., Hamada, S., et al. 2012, *ApJ*, 752, 15, doi: [10.1088/0004-637X/752/1/15](https://doi.org/10.1088/0004-637X/752/1/15)

Opitom, C., Snodgrass, C., Jehin, E., et al. 2025, *MNRAS*, 544, L31, doi: [10.1093/mnrasl/slaf095](https://doi.org/10.1093/mnrasl/slaf095)

Pinilla-Alonso, N., Brunetto, R., De Prá, M. N., et al. 2025, *Nature Astronomy*, 9, 230, doi: [10.1038/s41550-024-02433-2](https://doi.org/10.1038/s41550-024-02433-2)

Pontoppidan, K. M., Salyk, C., Banzatti, A., et al. 2024, *ApJ*, 963, 158, doi: [10.3847/1538-4357/ad20f0](https://doi.org/10.3847/1538-4357/ad20f0)

Quirico, E., Bacmann, A., Wolters, C., et al. 2023, *Icar*, 394, 115396, doi: [10.1016/j.icarus.2022.115396](https://doi.org/10.1016/j.icarus.2022.115396)

Rahatgaonkar, R., Carvajal, J. P., Puzia, T. H., et al. 2025, *ApJL*, 995, L34, doi: [10.3847/2041-8213/ae1cbc](https://doi.org/10.3847/2041-8213/ae1cbc)

Regan, M. 2024, Detection and Flagging of Showers and Snowballs in JWST, JWST-STScI-008545. https://www.stsci.edu/files/live/sites/www/files/home/jwst/documentation/technical-documents/_documents/JWST-STScI-008545.pdf

Rivkin, A. S., Thomas, C. A., Wong, I., et al. 2023, *PSJ*, 4, 214, doi: [10.3847/PSJ/ad04d8](https://doi.org/10.3847/PSJ/ad04d8)

Roth, N. X., Cordiner, M. A., Bockelée-Morvan, D., et al. 2025, arXiv, arXiv:2511.20845, doi: [10.48550/arXiv.2511.20845](https://doi.org/10.48550/arXiv.2511.20845)

Salazar Manzano, L. E., Lin, H. W., Taylor, A. G., et al. 2025, *ApJL*, 993, L23, doi: [10.3847/2041-8213/ae1232](https://doi.org/10.3847/2041-8213/ae1232)

Santana-Ros, T., Ivanova, O., Mykhailova, S., et al. 2025, *A&A*, 702, L3, doi: [10.1051/0004-6361/202556717](https://doi.org/10.1051/0004-6361/202556717)

Schaller, E. L., & Brown, M. E. 2007, *ApJL*, 659, L61, doi: [10.1086/516709](https://doi.org/10.1086/516709)

Seligman, D. Z., Micheli, M., Farnocchia, D., et al. 2025, *ApJL*, 989, L36, doi: [10.3847/2041-8213/adf49a](https://doi.org/10.3847/2041-8213/adf49a)

Tan, H., Yan, X., & Li, J.-Y. 2026, arXiv e-prints, arXiv:2601.15443, doi: [10.48550/arXiv.2601.15443](https://doi.org/10.48550/arXiv.2601.15443)

Taylor, A. G., & Seligman, D. Z. 2025, *ApJL*, 990, L14, doi: [10.3847/2041-8213/adfa28](https://doi.org/10.3847/2041-8213/adfa28)

Villanueva, G. L., Liuzzi, G., Faggi, S., et al. 2022, Fundamentals of the Planetary Spectrum Generator

Villanueva, G. L., Mumma, M. J., DiSanti, M. A., et al. 2011, *Icar*, 216, 227, doi: [10.1016/j.icarus.2011.08.024](https://doi.org/10.1016/j.icarus.2011.08.024)

Villanueva, G. L., Smith, M. D., Protopapa, S., Faggi, S., & Mandell, A. M. 2018, *JQSRT*, 217, 86, doi: [10.1016/j.jqsrt.2018.05.023](https://doi.org/10.1016/j.jqsrt.2018.05.023)

Virtanen, P., Gommers, R., Oliphant, T. E., et al. 2020, *NatMe*, 17, 261, doi: [10.1038/s41592-019-0686-2](https://doi.org/10.1038/s41592-019-0686-2)

Wells, M., Pel, J.-W., Glasse, A., et al. 2015, *PASP*, 127, 646, doi: [10.1086/682281](https://doi.org/10.1086/682281)

Wong, I. 2025, *jwstspec*, v0.6., Zenodo, doi: [10.5281/zenodo.1718639](https://doi.org/10.5281/zenodo.1718639)

Wong, I., Brown, M. E., Emery, J. P., et al. 2024, *PSJ*, 5, 87, doi: [10.3847/PSJ/ad2fc3](https://doi.org/10.3847/PSJ/ad2fc3)

Woodward, C. E., Bockelée-Morvan, D., Harker, D. E., et al. 2025, *PSJ*, 6, 139, doi: [10.3847/PSJ/add1d5](https://doi.org/10.3847/PSJ/add1d5)

Xing, Z., Oset, S., Noonan, J., & Bodewits, D. 2025, *ApJL*, 991, L50, doi: [10.3847/2041-8213/ae08ab](https://doi.org/10.3847/2041-8213/ae08ab)

Yang, B., Meech, K. J., Connelley, M., Zhao, R., & Keane, J. V. 2025, *ApJL*, 992, L9, doi: [10.3847/2041-8213/ae08a7](https://doi.org/10.3847/2041-8213/ae08a7)

Ye, Q., Kelley, M. S. P., Hsieh, H. H., et al. 2025, *ApJL*, 993, L31, doi: [10.3847/2041-8213/ae147b](https://doi.org/10.3847/2041-8213/ae147b)

Zhang, Q., & Battams, K. 2025, arXiv, arXiv:2510.25035, doi: [10.48550/arXiv.2510.25035](https://doi.org/10.48550/arXiv.2510.25035)